

# Characterizing the Infall Times and Quenching Timescales of Milky Way Satellites with *Gaia* Proper Motions

Sean P. Fillingham,<sup>1\*</sup> M. C. Cooper,<sup>1</sup> Tyler Kelley,<sup>1</sup> M. K. Rodriguez Wimberly,<sup>1</sup>  
Michael Boylan-Kolchin,<sup>2</sup> James S. Bullock,<sup>1</sup> Shea Garrison-Kimmel,<sup>3</sup>  
Marcel S. Pawlowski,<sup>4,1</sup> † ‡ Coral Wheeler<sup>3</sup>

<sup>1</sup>Center for Cosmology, Department of Physics & Astronomy, University of California, Irvine, 4129 Reines Hall, Irvine, CA 92697, USA

<sup>2</sup>Department of Astronomy, The University of Texas at Austin, 2515 Speedway, Stop C1400, Austin, TX 78712, USA

<sup>3</sup>TAPIR, Mailcode 350-17, California Institute of Technology, Pasadena, CA 91125, USA

<sup>4</sup>Leibniz-Institut für Astrophysik Potsdam (AIP), An der Sternwarte 16, D-14482 Potsdam, Germany

12 June 2019

## ABSTRACT

Observations of low-mass satellite galaxies in the nearby Universe point towards a strong dichotomy in their star-forming properties relative to systems with similar mass in the field. Specifically, satellite galaxies are preferentially gas poor and no longer forming stars, while their field counterparts are largely gas rich and actively forming stars. Much of the recent work to understand this dichotomy has been statistical in nature, determining not just that environmental processes are most likely responsible for quenching these low-mass systems but also that they must operate very quickly after infall onto the host system, with quenching timescales  $\lesssim 2$  Gyr at  $M_\star \lesssim 10^8 M_\odot$ . This work utilizes the newly-available *Gaia* DR2 proper motion measurements along with the Phat ELVIS suite of high-resolution, cosmological, zoom-in simulations to study low-mass satellite quenching around the Milky Way on an object-by-object basis. We derive constraints on the infall times for 37 of the known low-mass satellite galaxies of the Milky Way, finding that  $\gtrsim 70\%$  of the “classical” satellites of the Milky Way are consistent with the very short quenching timescales inferred from the total population in previous works. The remaining classical Milky Way satellites have quenching timescales noticeably longer, with  $\tau_{\text{quench}} \sim 6 - 8$  Gyr, highlighting how detailed orbital modeling is likely necessary to understand the specifics of environmental quenching for individual satellite galaxies. Additionally, we find that the 6 ultra-faint dwarf galaxies with publicly available *HST*-based star-formation histories are all consistent with having their star formation shut down prior to infall onto the Milky Way – which, combined with their very early quenching times, strongly favors quenching driven by reionization.

**Key words:** Local Group – galaxies: dwarf – galaxies: evolution – galaxies: star formation – galaxies: formation – galaxies: general

## 1 INTRODUCTION

Large surveys of the nearby Universe demonstrate that galaxies at (and below) the mass scale of the Magellanic clouds ( $10^6 M_\odot \lesssim M_\star \lesssim 10^9 M_\odot$ ) are predominantly star forming in the field (Haines et al. 2008; Geha et al. 2012). This stands in stark contrast to the population of low-mass galaxies that currently reside near a more massive host system, where the fraction of systems that are no longer forming stars (i.e. “quenched”) is significantly larger (Weinmann et al. 2006; Geha et al. 2012; Phillips et al. 2015). For dwarfs with

$M_\star \lesssim 10^8 M_\odot$  in the Local Volume, this field-satellite dichotomy is very apparent, with satellites of the Milky Way (MW) and M31 being largely gas-poor, passive systems in contrast to the gas-rich, star-forming field population (e.g. Mateo 1998; Greulich & Putman 2009; Spekkens et al. 2014). This clear distinction between the field and satellite populations strongly favors environmental processes as the dominant quenching mechanisms in this low-mass regime ( $M_\star \lesssim 10^8 M_\odot$ , Lin & Faber 1983; Slater & Bell 2014; Weisz et al. 2015; Wetzel et al. 2015b; Fillingham et al. 2015, 2016, 2018; Simpson et al. 2018). At the very lowest mass scales (i.e. the regime of ultra-faint dwarfs), however, there is evidence for a transition in the dominant quenching mechanism from one associated with galaxy environment to one driven by reionization. The universally old stellar populations observed in the ultra-faint dwarfs (UFDs)

\* e-mail: sfilling@uci.edu

† Schwarzschild Fellow

‡ Hubble Fellow

suggest that star formation on the smallest galactic scales is suppressed at very early times, favoring a transition in the dominant quenching mechanism at  $M_{\star} \lesssim 10^5 M_{\odot}$  (Brown et al. 2014; Rodriguez Wimberly et al. 2019).

Across all mass scales, some of the most powerful studies of satellite quenching have utilized measurements of satellite and field quenched fractions to infer the timescale upon which satellite quenching occurs following infall (e.g. Wetzel et al. 2013; Fillingham et al. 2015; Balogh et al. 2016; Fossati et al. 2017). These studies point to a picture where quenching proceeds relatively slowly at high satellite masses, consistent with quenching via starvation (Wheeler et al. 2014; Fillingham et al. 2015; Davies et al. 2016; Trussler et al. 2018). Below some host-dependent critical mass scale, however, quenching is rapid, as stripping becomes increasingly efficient (Fillingham et al. 2016). In defining this model of satellite quenching, simulations are commonly utilized to constrain the distribution of infall times for an observed sample of satellites. This statistical approach is required, as it is extremely difficult to infer the infall time for a significant fraction of the satellite population in even the most nearby groups and clusters. Moreover, in systems more distant than  $\sim 1$  Mpc, it is difficult to measure a precise star-formation history via spatially-resolved stellar photometry, even with the aid of imaging from the *Hubble Space Telescope* (*HST*). Within the Local Group, however, we are afforded the luxury of more detailed observations of the nearby satellite and field populations. This is particularly true with the release of *Gaia* Data Release 2 (DR2, Gaia Collaboration et al. 2016a, 2018a), which now enables an investigation of satellite quenching timescales (measured relative to infall) on an object-by-object basis. This offers a unique opportunity to test the results of large statistical analyses and our current physical picture of satellite quenching.

In this work, we aim to determine the quenching timescale and ultimately constrain the potential mechanisms responsible for suppressing star formation in individual MW satellite galaxies. Utilizing the latest data products from *Gaia* DR2 (Gaia Collaboration et al. 2018a,b), we infer the cosmic time when each dwarf galaxy around the MW became a satellite (i.e. the infall time) through comparison to the Phat ELVIS suite of cosmological zoom-in simulations of MW size galaxies (Kelley et al. 2018). In addition, we infer the quenching times for the MW satellites based on their published star-formation histories, as derived from *HST* imaging (Weisz et al. 2014, 2015; Brown et al. 2014). Finally, through comparison of the quenching times to the infall times, we characterize the quenching timescales for each object and constrain the potential mechanisms responsible for quenching each MW satellite galaxy. In §2, we discuss our sample of local dwarfs and the methodology by which we measure the infall and quenching time for each system. Our primary results are presented in §3, followed by a discussion of how these results connect to physical models of satellite quenching in §4. Finally, we summarize our results and conclusions in §5. Where necessary, we adopt a  $\Lambda$ CDM cosmology with the following parameters:  $\sigma_8 = 0.815$ ,  $\Omega_m = 0.3121$ ,  $\Omega_{\Lambda} = 0.6879$ ,  $n_s = 0.9653$ , and  $h = 0.6751$  (Planck Collaboration et al. 2016), consistent with the simulations used in this work.

## 2 MILKY WAY DWARF GALAXIES

As shown in Table 1, our sample of Milky Way satellite galaxies is selected from Fritz et al. (2018), totalling 37 systems located within 300 kpc of the MW and for which the *Gaia* DR2 dataset yields a proper motion measurement. Combined with mea-

surements of distance and line-of-sight velocity from the literature, the *Gaia* observations constrain the Galactocentric position and 3D velocity of each system (i.e. full 6D phase-space information). For those galaxies located within a Galactocentric distance of 300 kpc (i.e. within what we assume to be the virial radius of the MW), *HST*/WFPC2 and ACS imaging of 15 systems yields estimates of their star-formation history. These 15 dwarfs comprise our primary sample, spanning a stellar mass range of  $M_{\star} \sim 10^{3.5-8} M_{\odot}$ . All of the systems show no evidence of ongoing star formation, with minimal H I reservoirs ( $M_{\text{H I}} / M_{\star} < 0.1$ , Grcevich & Putman 2009; Spekkens et al. 2014). While this sample is undoubtedly incomplete below  $M_{\star} \sim 10^{5.5} M_{\odot}$  (Irwin 1994; Tollerud et al. 2008), particularly at large Galactocentric distances, our analysis focuses on the potential quenching mechanism for each system individually, such that it does not rely strongly on uniformly sampling the MW satellite population. Another source of incompleteness is expected to be the limited sky coverage of imaging surveys such as the Sloan Digital Sky Survey (York et al. 2000) and the Dark Energy Survey (Dark Energy Survey Collaboration et al. 2016), which should not be significantly correlated with the accretion history of the satellite population.

To better constrain the physical mechanisms responsible for quenching the low-mass satellites of the Milky Way, we aim to characterize the quenching timescale for each system. As we define more explicitly below, the quenching timescale is the difference between the infall time and the quenching time — i.e. the time that a satellite spends inside the host dark matter halo, following infall, prior to having its star formation shut down. To infer the quenching timescale, we must first measure the quenching time and infall time for each galaxy in our sample.

### 2.1 Quenching Time

A galaxy’s star-formation history (SFH) provides a direct constraint on the epoch at which a galaxy quenched. For nearby systems, where the stellar population can be resolved and imaging can reach the oldest main sequence turn-off population, we can constrain the SFH with relative precision (Dolphin 1997; Weisz et al. 2011). Here, we adopt the lookback time at which a galaxy forms 90% of its present day stellar mass ( $t_{90}$ ) to be the quenching time. Following Weisz et al. (2015), we utilize  $t_{90}$  (versus  $t_{100}$ ) to minimize the potential uncertainty associated with the modeling of blue straggler populations.

For 15 of the dwarfs in our sample (see Table 1), there are published star-formation histories from Weisz et al. (2014) and Brown et al. (2014), based on *HST*/WFPC2 and ACS imaging. In the case of three systems (all UFDs), the SFH is measured by both Brown et al. (2014) and Weisz et al. (2014), with excellent agreement between the two datasets for Hercules and Leo IV. For the third dwarf in common (CVn II), Weisz et al. (2014) find a more extended SFH, in contrast to the largely ancient stellar population inferred by Brown et al. (2014). Given that the *HST*/WFPC2 imaging analyzed by Weisz et al. (2014) is shallower and covers a smaller area than the *HST*/ACS imaging employed by Brown et al. (2014), we opt to utilize the SFH from Brown et al. (2014). Even allowing for the more extended SFH measured by Weisz et al. (2014), our results are qualitatively unchanged, such that we find CVn II quenches prior to infall. It should be noted that recent simulations of dwarf galaxies have found that stellar age gradients can exist and depend strongly on the SFH and merger history of an individual dwarf galaxy (El-Badry et al. 2016; Graus et al. 2019). These gradients can introduce an observational bias that varies depending on the location of the

Name	Distance (kpc)	$V_{3D}$ (km/s)	$V_r$ (km/s)	$V_{tan}$ (km/s)	$e$	$t_{90}$ (Gyr)	$t_{infall}$ (Gyr)
	(1)	(2)	(3)	(4)	(5)	(6)	(7)
Sag I	18	$312^{+21}_{-18}$	$142 \pm 1$	$278^{+23}_{-20}$	$0.42^{+0.03}_{-0.02}$	$3.4^{+5.2}_{-3.1}$	$10.6^{+1.6}_{-1.9}$
Tuc III	21	$-236^{+5}_{-5}$	$-228 \pm 2$	$60^{+12}_{-12}$	$0.86^{+0.03}_{-0.03}$	---	$9.5^{+2.4}_{-2.8}$
Dra II	23	$-355^{+25}_{-24}$	$-155 \pm 8$	$319^{+27}_{-27}$	$0.53^{+0.07}_{-0.06}$	---	$10.2^{+1.8}_{-2.4}$
Hyd I	25	$-370^{+14}_{-13}$	$-57 \pm 2$	$365^{+14}_{-13}$	$0.49^{+0.06}_{-0.05}$	---	$9.4^{+1.7}_{-1.8}$
Seg 1	27	$232^{+28}_{-26}$	$116 \pm 4$	$200^{+31}_{-30}$	$0.39^{+0.06}_{-0.04}$	---	$10.8^{+1.3}_{-1.4}$
Car III	28	$387^{+33}_{-30}$	$45 \pm 4$	$384^{+33}_{-30}$	$0.58^{+0.12}_{-0.11}$	---	$7.6^{+3.4}_{-2.7}$
Ret II	32	$-248^{+15}_{-14}$	$-102 \pm 2$	$226^{+17}_{-16}$	$0.31^{+0.02}_{-0.02}$	---	$10.2^{+1.1}_{-2.4}$
Tri II	34	$-333^{+20}_{-18}$	$-255 \pm 3$	$213^{+29}_{-28}$	$0.71^{+0.02}_{-0.02}$	---	$9.5^{+1.5}_{-2.1}$
Car II	37	$355^{+16}_{-14}$	$203 \pm 3$	$291^{+19}_{-18}$	$0.64^{+0.04}_{-0.03}$	---	$7.9^{+2.5}_{-2.4}$
Boo II	39	$-383^{+76}_{-68}$	$-54 \pm 9$	$378^{+79}_{-70}$	$0.63^{+0.28}_{-0.27}$	---	$1.1^{+0.6}_{-0.6}$
U Maj II	40	$-288^{+21}_{-19}$	$-58 \pm 2$	$282^{+21}_{-19}$	$0.26^{+0.1}_{-0.05}$	---	$10.7^{+1.4}_{-2.3}$
Seg 2	42	$224^{+39}_{-34}$	$73 \pm 3$	$211^{+40}_{-35}$	$0.27^{+0.09}_{-0.04}$	---	$10.8^{+1.6}_{-1.9}$
Wil I	42	$120^{+56}_{-44}$	$23 \pm 4$	$118^{+57}_{-47}$	$0.54^{+0.21}_{-0.24}$	---	$10.7^{+1.3}_{-1.4}$
ComBer I	43	$276^{+30}_{-27}$	$31 \pm 3$	$274^{+31}_{-28}$	$0.2^{+0.13}_{-0.06}$	$13.0^{+14.3}_{-11.8}$	$10.2^{+2.6}_{-3.3}$
Tuc II	53	$-283^{+24}_{-20}$	$-187 \pm 2$	$212^{+33}_{-29}$	$0.58^{+0.03}_{-0.02}$	---	$9.5^{+2.0}_{-1.9}$
Boo I	63	$192^{+27}_{-25}$	$94 \pm 2$	$167^{+32}_{-31}$	$0.41^{+0.12}_{-0.08}$	$12.6^{+13.7}_{-11.6}$	$10.7^{+0.6}_{-1.9}$
U Min I	77	$-153^{+17}_{-16}$	$-71 \pm 2$	$135^{+19}_{-19}$	$0.49^{+0.07}_{-0.08}$	$10.2^{+11.7}_{-7.7}$	$10.7^{+1.7}_{-2.0}$
Dra I	79	$-160^{+19}_{-15}$	$-88 \pm 2$	$133^{+22}_{-19}$	$0.53^{+0.07}_{-0.09}$	$9.1^{+10.7}_{-5.8}$	$10.4^{+2.4}_{-3.1}$
Hor I	83	$-213^{+48}_{-44}$	$-34 \pm 3$	$210^{+49}_{-44}$	$0.21^{+0.18}_{-0.08}$	---	$8.8^{+1.8}_{-2.0}$
Scu I	84	$198^{+21}_{-22}$	$74 \pm 1$	$184^{+22}_{-24}$	$0.32^{+0.07}_{-0.04}$	$10.6^{+11.9}_{-7.1}$	$9.9^{+1.7}_{-2.9}$
Sext I	88	$241^{+25}_{-22}$	$79 \pm 1$	$228^{+27}_{-23}$	$0.3^{+0.07}_{-0.02}$	---	$8.4^{+2.7}_{-0.9}$
U Maj I	101	$257^{+62}_{-53}$	$9 \pm 2$	$257^{+62}_{-53}$	$0.31^{+0.34}_{-0.22}$	$11.2^{+12.5}_{-10.0}$	$1.5^{+5.1}_{-1.6}$
Aqu II	105	$250^{+241}_{-164}$	$49 \pm 8$	$244^{+242}_{-174}$	$0.75^{+0.24}_{-0.45}$	---	$1.6^{+5.4}_{-3.5}$
Car I	105	$162^{+21}_{-22}$	$1 \pm 2$	$162^{+21}_{-22}$	$0.27^{+0.12}_{-0.12}$	$2.2^{+3.7}_{-2.2}$	$9.9^{+0.6}_{-2.7}$
Cra II	111	$-113^{+24}_{-19}$	$-83 \pm 2$	$75^{+34}_{-35}$	$0.74^{+0.13}_{-0.15}$	---	$7.8^{+2.7}_{-2.0}$
Gru I	116	$-274^{+102}_{-69}$	$-195 \pm 4$	$190^{+127}_{-117}$	$0.81^{+0.17}_{-0.11}$	---	$1.1^{+1.0}_{-0.9}$
Her I	128	$163^{+31}_{-9}$	$152 \pm 1$	$59^{+61}_{-37}$	$0.85^{+0.1}_{-0.18}$	$11.8^{+13.2}_{-10.5}$	$6.6^{+2.3}_{-0.7}$
Frn I	141	$-137^{+26}_{-25}$	$-41 \pm 1$	$131^{+27}_{-27}$	$0.42^{+0.14}_{-0.13}$	---	$10.7^{+0.8}_{-3.1}$
Cra I	144	$-112^{+133}_{-77}$	$-10 \pm 3$	$111^{+132}_{-79}$	$0.63^{+0.31}_{-0.38}$	---	$8.9^{+3.0}_{-3.1}$
Hyd II	147	$284^{+259}_{-141}$	$118 \pm 6$	$257^{+272}_{-177}$	$0.89^{+0.1}_{-0.36}$	$2.2^{+2.5}_{-2.0}$	$10.5^{+1.5}_{-2.4}$
Leo IV	154	$312^{+306}_{-217}$	$1 \pm 8$	$311^{+306}_{-217}$	$0.95^{+0.05}_{-0.62}$	$12.2^{+13.6}_{-10.7}$	$10.4^{+1.4}_{-1.4}$
CVn II	160	$-182^{+150}_{-77}$	$-93 \pm 4$	$157^{+163}_{-108}$	$0.71^{+0.27}_{-0.26}$	$12.7^{+14.3}_{-11.1}$	$9.0^{+1.0}_{-2.8}$
Leo V	173	$311^{+307}_{-210}$	$50 \pm 7$	$308^{+309}_{-219}$	$0.96^{+0.04}_{-0.58}$	---	$10.6^{+1.4}_{-1.5}$
Pis II	181	$-400^{+434}_{-265}$	$-64 \pm 8$	$394^{+438}_{-275}$	$0.99^{+0.01}_{-0.48}$	---	$8.3^{+1.8}_{-1.8}$
CVn I	210	$125^{+67}_{-38}$	$81 \pm 2$	$94^{+78}_{-62}$	$0.66^{+0.24}_{-0.25}$	$8.3^{+9.5}_{-6.3}$	$9.4^{+0.9}_{-2.3}$
Leo II	227	$76^{+77}_{-44}$	$19 \pm 1$	$74^{+78}_{-49}$	$0.73^{+0.2}_{-0.44}$	$6.4^{+7.2}_{-5.8}$	$7.8^{+3.3}_{-2.0}$
Leo I	272	$181^{+44}_{-13}$	$166 \pm 1$	$71^{+79}_{-48}$	$0.87^{+0.09}_{-0.09}$	$1.7^{+1.9}_{-1.6}$	$2.3^{+0.6}_{-0.5}$

**Table 1.** Properties of satellite galaxies of the Milky Way, as selected from [Fritz et al. \(2018\)](#) and listed in order of increasing Galactocentric distance. (1) Distance from the center of the MW in kpc ([Fritz et al. 2018](#)). (2) Total velocity, (3) Radial velocity, and (4) Tangential velocity, all in  $\text{km s}^{-1}$ , in the Galactocentric frame-of-reference ([Fritz et al. 2018](#)). (5) Orbital eccentricity,  $e$ , based on the “heavy” MW mass used in [Fritz et al. \(2018\)](#). (6) Quenching time ( $t_{90}$ ), in Gyr, inferred from published SFHs by adopting the lookback time at which the dwarf galaxy formed 90% of its current stellar mass ([Weisz et al. 2014](#); [Brown et al. 2014](#)). The uncertainty on  $t_{90}$  as given by the  $1\sigma$  bounds on the quenching time, in Gyr, inferred from the SFHs by adopting the lookback-time at which the  $1\sigma$  bounds on the SFH crossed the 90% mass threshold. (7) Infall time, in Gyr, inferred from the peak in the infall time KDE from matching to subhalos in the pELVIS simulations (see §2.2). The uncertainty in the infall time, in Gyr, as given by the upper and lower bounds on the KDE that encompass 68% of the distribution centered on the peak, or roughly  $1\sigma$  (see the magenta shaded region in Figure 2). This table will be available at <https://sfillingham.github.io> after the paper is accepted for publication.

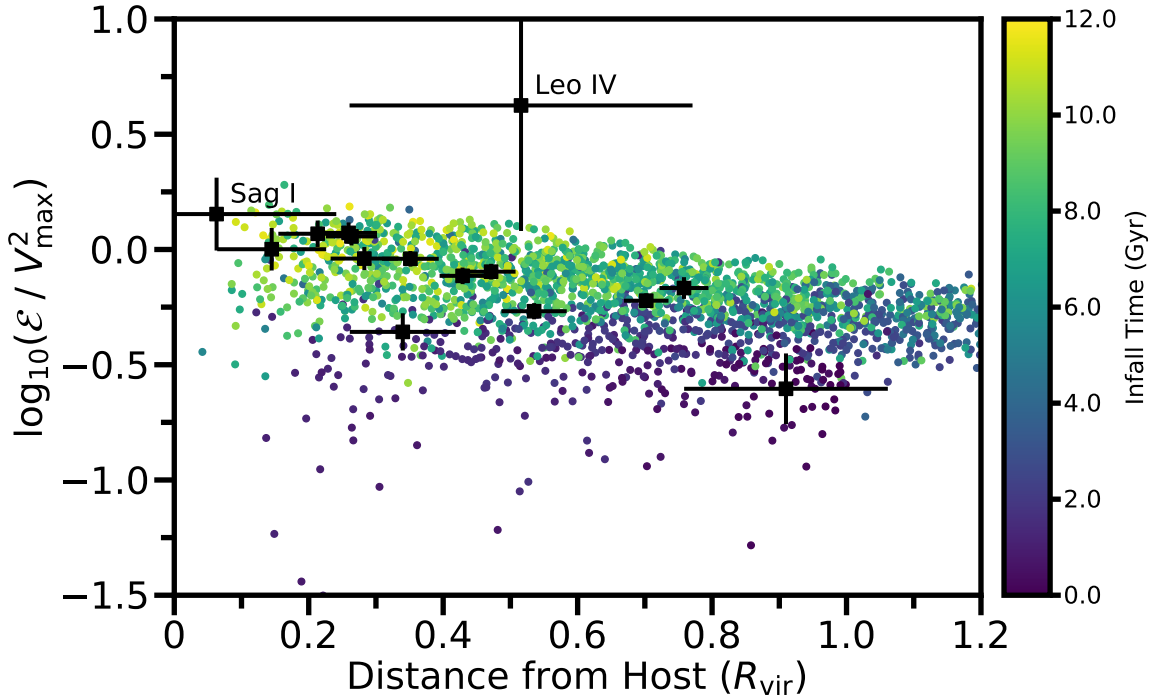


**Figure 1.** The binding energy ( $\mathcal{E}$ ), scaled by the present-day  $V_{\max}$  of the host, as a function of distance from the host (in units of host  $R_{\text{vir}}$ ) for subhalos in the pELVIS simulation suite. Each point is color-coded by the lookback time to first infall for the subhalo. The black squares correspond to the Milky Way satellites in our primary sample, assuming  $M_{\text{vir}} = 1.3 \times 10^{12} M_{\odot}$ ,  $R_{\text{vir}} = 300$  kpc,  $R_s = 18.75$  kpc, and  $V_{\max} = 200$  km/s. To constrain  $t_{\text{infall}}$ , we select the 15 subhalos closest to each MW dwarf in the plotted parameter space, restricting to only those subhalos that also have the same directionality in their host-centric radial velocity component. The error bars illustrate the selection region for each MW dwarf based on this selection criteria (see §2 for more details). There exists a strong gradient in typical infall time within this parameter space. Many of the Milky Way satellites reside in regions with well-defined infall times, such that strong constraints can be placed on  $t_{\text{infall}}$ . Two objects, Sag I and Leo IV, are not well matched in this analysis, see §4 for a more detailed discussion.

*HST* field relative to the galaxy half-light radius, with the potential to shift the inferred median stellar age by as much as  $\pm 2$  Gyr (Graus et al. 2019). For the SFHs from Weisz et al. (2014) and Brown et al. (2014), the corresponding *HST* imaging fields are, on average, biased towards the center of each system, so as to weakly favor younger SFHs and thus slightly underestimate  $t_{90}$ .

To determine the time at which each system formed 90% of its stellar mass ( $t_{90}$ ), we linearly interpolate the measured SFHs from Weisz et al. (2014), using the published data tables (Weisz et al. 2017). As shown in Figure 2 for Leo II, the corresponding uncertainty in  $t_{90}$  is determined by similarly interpolating and evaluating the SFHs including their associated  $1\sigma$  random and systematic errors. For the remaining 6 systems in our sample, we visually inspect the published SFHs from Brown et al. (2014) to measure  $t_{90}$ . In particular, utilizing the  $1\sigma$  confidence intervals from Figure 8 of Brown et al. (2014), we select the lookback time at which the upper and lower bounds of the SFH reach 90% of the present day mass of the system. The average of these two times is taken to be  $t_{90}$ . For Hercules and Leo IV, we find a very minor difference between the  $t_{90}$  inferred from using the Weisz et al. (2014) dataset and from visually inspecting the Brown et al. (2014) results ( $\Delta t_{90} \lesssim 1$  Gyr). The  $t_{90}$  measurements for each system in our sample, which we take to be the quenching time ( $t_{\text{quench}}$ ), are listed in Table 1 along with their corresponding uncertainties.

## 2.2 Infall Time

For low-mass dwarfs in the Local Volume, there is a stark difference in the star-forming properties of those within the virial radius ( $\sim 300$  kpc) of either the MW or M31 and those in the field (e.g. Spekkens et al. 2014). While it is uncertain as to the exact physical scale at which environmental effects begin to affect satellite galaxies, this observed field-satellite dichotomy makes a strong case that infall onto the host system (as defined by crossing within the host's virial radius) marks the onset of environmental quenching. In order to constrain the timescale upon which environmental processes act (i.e. the quenching timescale), we must infer the infall time — i.e. the time at which a satellite crosses within the virial radius of the host — for each dwarf in our sample.

### 2.2.1 Gaia Proper Motions

The *Gaia* mission recently transformed the observational landscape, providing proper motion measurements for stars in a large number of local dwarfs (Gaia Collaboration et al. 2016a,b, 2018a). Using these data, several studies inferred proper motions for the Milky Way satellites, utilizing various membership criteria (Gaia Collaboration et al. 2018b; Simon 2018; Fritz et al. 2018; Kallivayalil et al. 2018; Massari & Helmi 2018; Pace & Li 2019). Here, we use the results from Fritz et al. (2018), as they provide the most comprehensive set of proper motion measures for the MW satellite population. For our primary sample, the observed proper motions

as measured by Fritz et al. (2018) agree (within the quoted errors) with those estimated by both Simon (2018) as well as Gaia Collaboration et al. (2018b). From Fritz et al. (2018), we adopt the Galactocentric distance, radial velocity, tangential velocity, 3D velocity, and eccentricity measures for each system (see Table 1). Using this phase-space information, we match the MW satellites to a subhalo population drawn from high-resolution, cosmological, zoom-in simulations in an effort to constrain their infall times. It should be noted that the proper motions (and resulting Galactocentric velocities) in some cases have very large uncertainties, which lead to an overestimation of the proper motion. We therefore expect that some of the objects in this analysis (e.g. Leo IV) will have unusually large Galactocentric velocities. Ultimately this uncertainty only affects Leo IV in our primary sample (see Fig. 1), and does not change our overall conclusions.

## 2.2.2 Simulations

To determine the infall time of each Milky Way satellite in our sample, we utilize the Phat ELVIS (pELVIS) suite of 12 high-resolution, dissipationless simulations of Milky Way-like halos along with an analytic potential set to match the observed properties of the MW disk and bulge (Kelley et al. 2018). The suite includes 12 isolated halos simulated within high-resolution uncontaminated volumes spanning 1 – 3 Mpc in size and using a particle mass of  $2.92 \times 10^4 M_\odot$  and a Plummer equivalent force softening of  $\epsilon = 25$  physical parsecs. Within the high-resolution volumes, the halo catalogs are complete down to  $M_{\text{halo}} > 3 \times 10^6 M_\odot$ ,  $V_{\text{max}} > 4.5 \text{ km s}^{-1}$ ,  $M_{\text{peak}} > 8 \times 10^6 M_\odot$ , and  $V_{\text{peak}} > 5 \text{ km s}^{-1}$  — therefore more than sufficient to track the evolution and infall time of halos hosting MW dwarfs with  $M_\star > 10^{3.5} M_\odot$  (Garrison-Kimmel et al. 2014). The simulations adopt a cosmological model with the following  $\Lambda$ CDM parameters:  $\sigma_8 = 0.815$ ,  $\Omega_m = 0.3121$ ,  $\Omega_\Lambda = 0.6879$ ,  $n_s = 0.9653$ , and  $h = 0.6751$  (Planck Collaboration et al. 2016). For a detailed discussion of the simulations and the impact of the host baryonic potential on the subhalo (i.e. satellite) population, we refer the reader to Kelley et al. (2018), see also D’Onghia et al. 2010; Garrison-Kimmel et al. 2017; Sawala et al. 2017; Graus et al. 2018).

For all subhalos with  $M_{\text{peak}} > 10^8 M_\odot$ , we determine their infall time, defined to be the first timestep when the subhalo passes within the host virial radius. Some ( $\sim 24\%$ ) of the subhalos have multiple infall times, with a median difference between first and last infall of 3.9 Gyr. These differences lead to a marginal change in the infall time inference for individual MW satellites ( $\sim 0.71$  Gyr), however they do not change the qualitative results of this work. On average, there are 250 subhalos per host above our adopted mass limit of  $M_{\text{peak}} > 10^8 M_\odot$ , with the 100% scatter ranging from 129 to 367. All of the subhalos from each simulation box are combined into one final catalog when compared to the MW satellite population.

To facilitate constraining the infall time for each MW dwarf galaxy, we match the observed 6D phase-space properties of the MW satellites to subhalo properties in the simulations. Using the measured infall time for each subhalo, we can map the infall time distributions to the phase-space distributions in the simulations. A useful method for mapping these two distributions is presented in Rocha et al. (2012), where a very strong correlation is found between the present-day binding energy of the subhalos in simulations and their infall times. We use a modified version of the subhalo binding energy presented in Rocha et al. (2012) in order to match the observed binding energies to the subhalo properties, thereby constraining the possible distribution of infall times for each MW satellite.

## 2.2.3 Binding Energy

As shown by Rocha et al. (2012), the binding energy per unit mass,  $\mathcal{E}$ , of a dark matter subhalo strongly correlates with its infall time, such that early accreted subhalos have higher binding energies. Following Rocha et al. (2012), we define the binding energy of a subhalo (or local dwarf) as

$$\mathcal{E} = -\phi(R) - \frac{1}{2}V^2, \quad (1)$$

where  $\phi(R)$  is the potential of the subhalo (or MW satellite) at the host-centric radial distance,  $R$ , and  $V^2/2$  corresponds to the kinetic energy of the subhalo (or galaxy), with  $V$  representing the magnitude of the 3D velocity vector in the frame of reference of the host.

To determine the potential of each satellite galaxy and subhalo, we assume the host mass is distributed in an NFW potential (Navarro et al. 1997):

$$\phi(r) = -4\pi G \rho_0 r_s^2 \frac{\ln(1 + r/r_s)}{r/r_s}, \quad (2)$$

where  $G$  is the gravitational constant,  $\rho_0$  is the average density of the dark matter halo, and  $r_s$  is the scale radius. We define  $\phi(R_0) = 0$  at  $R_0 = 5$  Mpc. Varying the distance where we anchor the potential does not significantly affect the binding energy measurement or the subsequent distribution of infall times for each MW satellite galaxy. Adopting  $R_0 = 5$  Mpc ensures that  $R_0$  is well outside the virial radius of the host for all of cosmic time. The simulations include hosts spanning a range of virial masses and we use their respective concentrations as given in Table 2 of the pELVIS halo catalogs (Kelley et al. 2018). These concentrations tend to be larger than their dark-matter-only counterparts owing to the response of the baryonic potential. For the suite of 12 hosts, the median concentration is  $c \sim 16$ .

Due the variation in the host virial masses across the simulation suite, the absolute normalization of the binding energy also varies from host to host. Essentially, the subhalos of more massive hosts have larger binding energies, on average, due to their deeper potentials. To better compare the simulations to the observational data, we combine the subhalo populations across the various simulation boxes. We “normalize” the binding energy of each satellite by dividing the measured binding energy by the present-day host maximum circular velocity squared ( $V_{\text{max}}^2$ ). For the MW dwarfs, we assume the host potential is an NFW with the following properties:  $M_{\text{vir}} = 1.3 \times 10^{12} M_\odot$ ,  $R_{\text{vir}} = 300$  kpc, and  $R_s = 18.75$  kpc (Bland-Hawthorn & Gerhard 2016).

## 2.2.4 Subhalo Matching

Both the binding energy, as defined in Equation 1, and the radial distance from the host are scalar quantities. By including the vector information (namely the direction of the radial velocity) associated with the satellite velocities, we endeavor to further constrain the inferred infall times using a two-step subhalo selection criteria – essentially a vector-based selection followed by a scalar-based selection. First, we select all subhalos with radial velocity components in the same direction as the dwarf galaxy in question (e.g. since Leo II has a positive radial velocity, we first select all of the subhalos that also have positive radial velocities). From the remaining subhalos, we select the 15 nearest to the Milky Way dwarf in the  $\log(\mathcal{E}/V_{\text{max}}^2)$ -versus- $R/R_{\text{vir}}$  space (see Figure 1).

For each sample of  $N = 15$  subhalos, we infer the underlying distribution of infall times through kernel density estimation

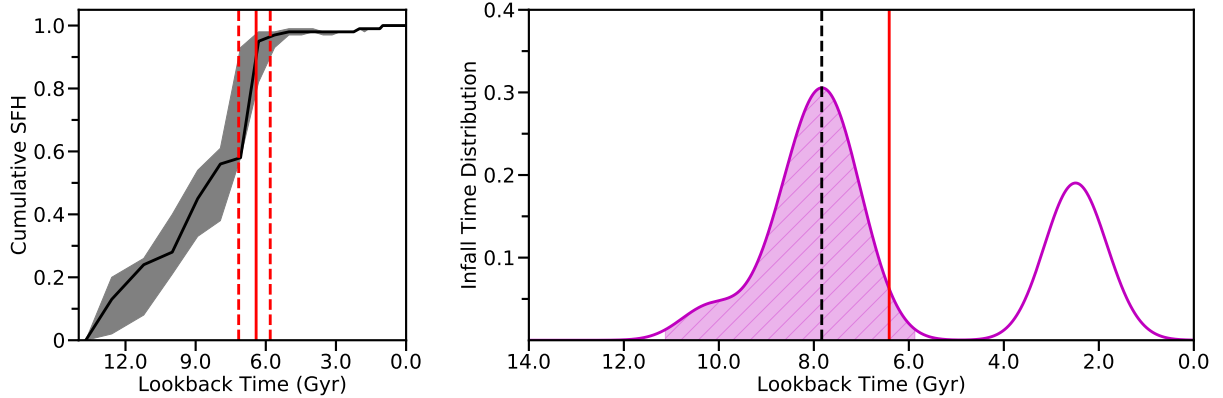


**Figure 2.** Illustrative example of both the quenching time and infall time measurements. *Left:* The cumulative SFH for Leo II, adapted from Weisz et al. (2014), showing the adopted quenching time (solid red line) and corresponding  $1\sigma$  uncertainty in the quenching time (dashed red lines). *Right:* The distribution of infall times for Leo II based on selecting the 15 subhalos that both reside nearest to Leo II in the  $\log(\mathcal{E}/V_{\max}^2)$ –host-centric distance space (see Fig. 1) and have the same directionality in their radial velocity. The  $t_{\text{infall}}$  KDE (magenta line) is inferred using a gaussian kernel with a bandwidth selected via a leave-one-out cross validation grid search. We adopt the peak in the distribution (black dashed line) as the characteristic infall time for Leo II. The accompanying magenta shaded region illustrates the bounds on the uncertainty in the inferred  $t_{\text{infall}}$ , corresponding to the most probable region encompassing 68 % of the total distribution. For reference, the red line shows the quenching time as derived from the star formation history in the *left* panel. The typical Leo II-like subhalo in the simulations falls onto the host system for the first time  $\sim 2$  Gyr prior to the cessation of star formation. This relatively fast quenching timescale is consistent with previous statistical work and favors ram-pressure stripping as the dominant quenching mechanism, perhaps assisted by tidal stripping and stellar feedback during pericentric passage.

(KDE). We adopt a gaussian kernel and select the bandwidth using a grid search with leave-one-out cross validation for each individual galaxy (e.g. Efron 1982). The peak in each KDE is adopted as the characteristic infall time for each MW dwarf galaxy. To estimate the uncertainty in the inferred infall time, we integrate the KDE, centered at the peak, until the bounds include 68% of the area under the curve, thereby approximating the  $1\sigma$  width of the distribution (see the magenta shaded region in Fig. 2 as an example).

We check the validity of this method by drawing a “test” sample from the simulation data and attempt to infer the true infall times of this subset using the methodology described above. By construction, the total sample includes the test subhalos, such that adopting a comparison set of  $N = 1$  (versus  $N = 15$ ) returns the exact subhalos in question and a “perfect” infall time inference. We estimate the accuracy of our methodology from the difference between the inferred infall time and the true infall time for the subhalo population. The distribution of differences in the infall time is sharply peaked at 0 Gyr with a standard deviation of  $\sim 1.0$  Gyr, suggesting that we are able to accurately constrain the true infall time for the majority of subhalos. It should be noted that exclusion of the vector information from our method increases the standard deviation to  $\sim 3.0$  Gyr, highlighting how using both the vector and scalar selections dramatically improves the accuracy of the inference. For each subhalo (or satellite), the resulting infall time distribution does not depend strongly on the choice of  $N = 15$  for  $5 < N < 20$ . We select  $N = 15$  so as to balance properly sampling the underlying distribution against sampling too much of the  $\log(\mathcal{E}/V_{\max}^2)$ -versus- $R/R_{\text{vir}}$  parameter space.

### 2.3 Quenching Timescale

As discussed previously, we define the quenching timescale ( $\tau_{\text{quench}}$ ) as the time that a satellite continues to form stars following infall. In other words, the quenching timescale is the difference

between the infall time and the quenching time:

$$\tau_{\text{quench}} = t_{\text{infall}} - t_{\text{quench}}, \quad (3)$$

where  $t_{\text{infall}}$  and  $t_{\text{quench}}$  are the lookback time to infall and quenching, respectively. In Table 1, we report the measured infall time for all dwarfs in the Fritz et al. (2018) sample within 300 kpc of the MW and the quenching time for each dwarf in our primary sample. The uncertainty in both the infall time and quenching time are added in quadrature to compute the total uncertainty in the quenching timescale.

## 3 RESULTS

Figure 3 shows the quenching time as a function of infall time, color-coded by stellar mass, for our primary sample of Milky Way satellites with published *HST*-based star-formation histories. For the lowest mass systems ( $M_{\star} \lesssim 10^5 M_{\odot}$ ), we find that the quenching time universally exceeds the infall time ( $t_{\text{quench}} > t_{\text{infall}}$ ), such that the suppression of star formation preceded infall onto the Milky Way. In contrast, at higher satellite masses, quenching is found to occur at (or after) the time of infall ( $t_{\text{quench}} \lesssim t_{\text{infall}}$ ). In this manner, the quenching time–infall time space can be used to determine the class of quenching mechanisms potentially responsible for shutting down star formation. Specifically, objects that fall below and to the right of the dashed line in Figure 3 are consistent with environmental quenching, where star formation is quenched after the galaxy becomes a satellite. The distance from the dashed line in combination with how early (or late) infall time occurred, can further constrain which environmental quenching mechanisms are most likely responsible. The horizontal dot-dashed line at  $t_{\text{quench}} = 12.5$  Gyr ( $z \sim 6$ ) marks the approximate location of the end of reionization (e.g. Fan et al. 2006; Robertson et al. 2015). Galaxies with  $t_{\text{quench}}$  consistent with this value are potentially quenched during (or shortly after) the epoch of reionization. The remaining region in the  $t_{\text{quench}}-t_{\text{infall}}$  space, above and to the left of the dashed line

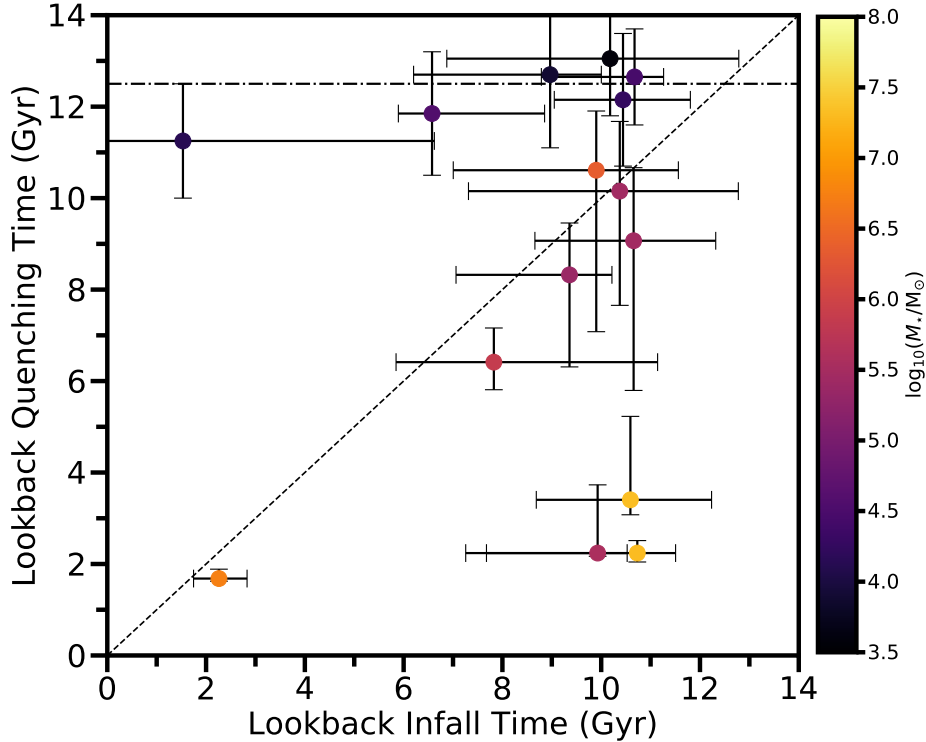


**Figure 3.** The relationship between quenching time ( $t_{\text{quench}}$ ) and infall time ( $t_{\text{infall}}$ ) for our primary sample of MW satellites. The points are color-coded by their present-day stellar mass, assuming  $M/L_V = 1$  (see color bar for scale). The low-mass ( $M_\star < 10^5 M_\odot$ ) satellites have quenching times consistent with suppression of star formation due to cosmic reionization, as illustrated by the dot-dashed line. For the “classical” ( $M_\star = 10^{5-8} M_\odot$ ) satellites, we generally find quenching and infall times that are consistent with a rapid cessation of star formation following accretion onto the MW. The lack of satellites with recent infall times is largely a consequence of observational bias, particularly at low stellar masses. Objects that recently fell onto the MW system preferentially reside at larger Galactocentric distances, such that we are likely “missing” a significant number of low-mass satellites for which we would infer more recent infall times. Finally, none of the satellites studied have quenching and infall times that strongly favor self-quenching via internal processes.

but below the dot-dashed line, favors quenching via feedback or some other internal process such that star formation is suppressed prior to infall. As evident in Fig. 3, this region of parameter space is largely unoccupied, suggesting that internal processes are not a primary driver of quenching within the low-mass galaxy population. This is consistent with observations of the field population, which is dominated by star-forming systems at these mass scales (Geha et al. 2012). Our measurements are very consistent with rapid quenching ( $\tau_{\text{quench}} \sim 1$  Gyr) within the MW halo at a  $< 2\sigma$  level.

Subtracting the quenching time from the infall time, we determine the quenching timescale ( $\tau_{\text{quench}}$ ) for every satellite galaxy in our primary sample (see Equation 3). In Figure 4, we plot this quenching timescale, for each system, as a function of its stellar mass (cyan hexagons). In addition, we include an estimate of the quenching timescale for the Small and Large Magellanic Clouds (SMC/LMC) as denoted by the magenta hexagon. Under the assumption that the SMC and LMC are on first infall, orbital modeling can estimate the lookback time at which they crossed the MW virial radius (Besla et al. 2007; Kallivayalil et al. 2013). We estimate the infall time for the Magellanic system to be  $\sim 1.5$  Gyr (Figure 13 of Kallivayalil et al. 2013), which leads to a conservative lower limit on the quenching timescale based on the framework described in this work. For comparison to the estimates of the quenching timescale for individual MW satellites, we also include the results of several statistical studies that provide estimates of the typical quenching

timescale for various satellite and host samples in the local Universe (Wetzel et al. 2013; Wheeler et al. 2014; Fillingham et al. 2015). Overall, the individual measures of  $\tau_{\text{quench}}$  for the MW satellites are in good agreement with the results based on the analysis of ensembles. At  $M_\star \gtrsim 10^5 M_\odot$ , the positive quenching timescales are broadly consistent with the expectations from Fillingham et al. (2015). Meanwhile, the universally negative quenching timescales for the lowest mass systems ( $M_\star \lesssim 10^5 M_\odot$ ) are consistent with quenching driven by reionization (Rodríguez Wimberly et al. 2019).

## 4 DISCUSSION

### 4.1 Quenching in Classical Dwarf Satellites

For decades now, the suppression of star formation in the “classical” dwarf galaxy population orbiting the MW ( $M_\star \sim 10^{5-8} M_\odot$ ) has been commonly attributed to processes associated with environment (e.g. Lin & Faber 1983; Blitz & Robishaw 2000). More recent modeling work shows that the timescale, over which the transition from star forming to quiescent must occur (following infall onto the host), is very short (Slater & Bell 2014; Wetzel et al. 2015a; Fillingham et al. 2015; Simpson et al. 2018). This short quenching timescale is consistent with ram-pressure stripping being the dominant quenching mechanism. In an effort to explicitly test the validity of this hypothesis, Fillingham et al. (2016) find that gas

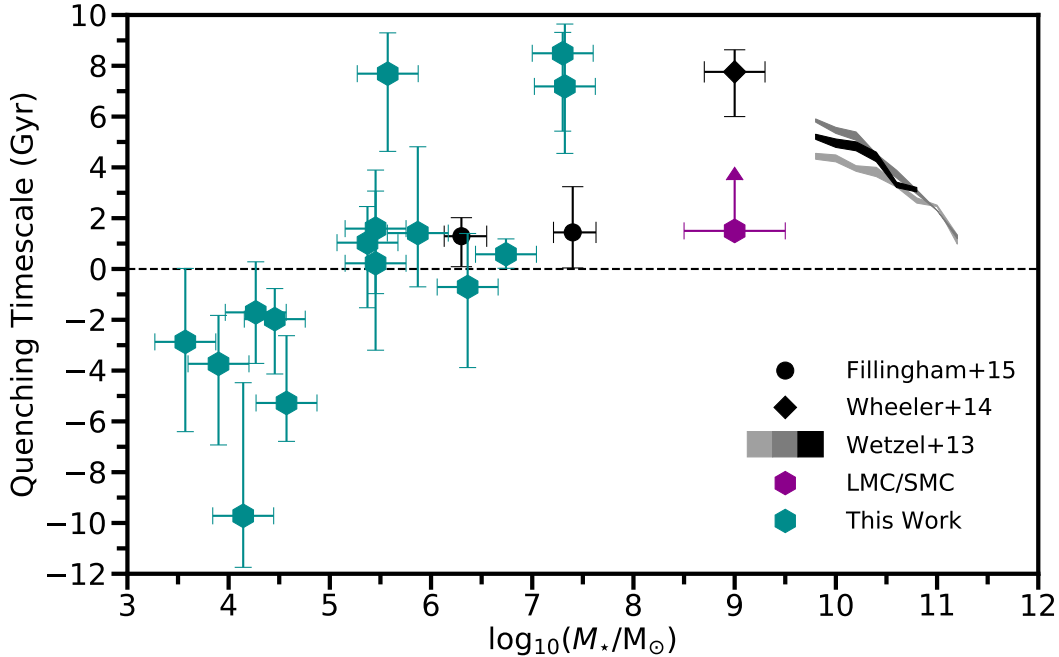


**Figure 4.** The quenching timescale as a function of satellite stellar mass for our primary sample of MW dwarfs (cyan hexagons). We include an estimate of the quenching timescale for both the SMC and LMC (magenta hexagon) based on a lookback time to first infall of 1.5 Gyr from Kallivayalil et al. (2013). The black data points and grey bands illustrate the results of statistical studies of satellites in groups and clusters (including the Local Group, Wetzel et al. 2013; Wheeler et al. 2014; Fillingham et al. 2015), with the grey bands corresponding to groups with estimated halo masses of  $10^{12-13}$ ,  $10^{13-14}$ , and  $10^{14-15} M_{\odot}$  (black, dark grey, and light grey, respectively). Our measured quenching timescales, computed on an object-by-object basis, are in general agreement with the results of statistical studies, such that satellites with  $10^5 \lesssim M_{\star}/M_{\odot} \lesssim 10^8$  have positive and short quenching timescales consistent with relatively rapid environmental quenching. Below this mass scale ( $M_{\star} \lesssim 10^5 M_{\odot}$ ), our measured quenching timescales are systematically negative, consistent with a scenario in which the lowest-mass galaxies quench prior to infall (i.e. at the time of, or shortly following, reionization).

stripping processes can reproduce the necessary timescales if the density of the MW circumgalactic medium (CGM) is clumpy (see Emerick et al. 2016, for a contrasting view), such that orbiting satellite galaxies will experience elevated ram-pressure stripping when they interact with these overdensities. The majority of classical MW satellite galaxies in this study are consistent with having their star formation shut down very rapidly after falling onto the MW system and becoming a satellite (i.e.  $\tau_{\text{quench}} \sim 1 - 2$  Gyr). These objects fit nicely into the environmental quenching picture put forward in Fillingham et al. (2015, 2016).

As evident in Figure 4, however, there are three dwarfs (Sagittarius, Fornax, and Carina) with inferred quenching timescales significantly longer than the short quenching timescales inferred from previous work. Closer inspection of Sag I suggests that its infall time (and thus quenching timescale) is not reliably measured via comparison to subhalos in the pELVIS simulation suite. As readily seen in Figure 1, Sag I occupies a region of the binding energy-vs-distance parameter space that is largely devoid of corresponding subhalos in the simulations. This is likely due to the fact that the pELVIS simulations do not account for the satellite’s baryonic component. In the case of a system such as Sag I that is being disrupted via tidal interaction with the MW, the corresponding subhalo population in the pELVIS simulations is quickly stripped, whereas Sag I is better able to resist disruption due to its non-negligible baryonic mass (Lazar et al., in prep). Put another way, at fixed host mass, low-mass subhalos are stripped more slowly (Boylan-Kolchin & Ma 2007;

Boylan-Kolchin et al. 2008), such that at small host-centric distance and high binding energy the subhalo population in pELVIS is dominated by low-mass subhalos that have been preferentially accreted at higher  $z$ . As a result, the measured infall time for Sag I, based on comparison to pELVIS, is biased towards early cosmic time. Previous work modeling the associated stellar stream suggests that Sag I was accreted onto the MW roughly  $\lesssim 2 - 8$  Gyr ago, following an orbit with a close pericentric passage ( $\lesssim 20$  kpc, Law & Majewski 2010; Purcell et al. 2011; Dierickx & Loeb 2017). If we assume  $t_{\text{infall}} \sim 5$  Gyr for Sag I, instead of our estimate of  $t_{\text{infall}} \sim 11$  Gyr, we find a quenching timescale of  $\tau_{\text{quenching}} \sim 1.6$  Gyr, consistent with rapid suppression of star formation following infall.

The other two satellites (Fornax and Carina), for which we measure  $\tau_{\text{quench}} > 4$  Gyr, suffer far less from the issues associated with modeling Sag I, such that the long quenching timescales inferred for these systems are much more reliable. These two systems, however, are outliers with regard to their orbits as inferred by Fritz et al. (2018) for the “heavy” MW potential. In Figure 5, we plot the measured quenching timescale as a function of orbital eccentricity, color-coded by pericentric distance, for those satellites in our primary sample with  $M_{\star} > 10^5 M_{\odot}$ . Among the massive satellites in our primary sample, Carina and Fornax have some of the lowest orbital eccentricities (i.e. the most circular orbits). In addition, Carina and Fornax are on orbits with relatively large pericenters of 60 and 58 kpc, respectively. Taken together, the orbital eccentricity and pericentric distance for Carina and Fornax are consistent with



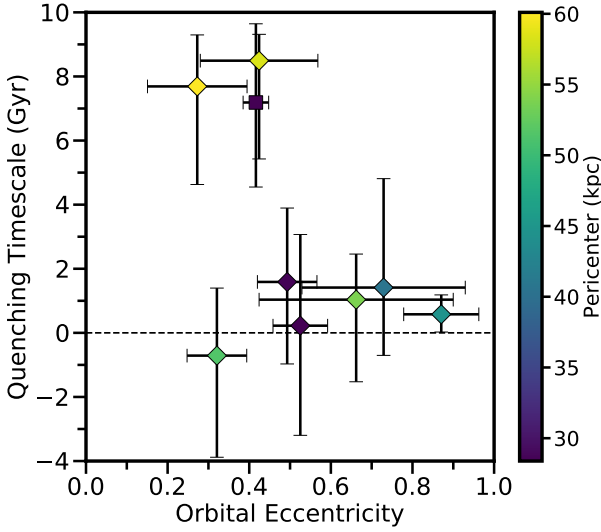


**Figure 5.** The quenching timescale as a function of orbital eccentricity, color-coded by pericentric distance, for the MW satellites with  $M_{\star} > 10^5 M_{\odot}$  in our primary sample. Due to the limitations of modeling Sag using the pELVIS simulations, it is given a different marker (square) to distinguish it from the other satellites (diamonds) in this analysis. The satellite galaxies with the longest quenching timescales are on orbits with some of the smallest eccentricities – i.e. more circular orbits. When combined with the relatively large pericentric distances for their orbits, these dwarf galaxies have likely experienced lower ram-pressure stripping, on average, allowing them to retain more of their cold gas reservoir and continue to form stars longer than satellites on more radial orbits.

orbits about the MW that would lead to less efficient quenching via environmental processes (e.g. ram-pressure stripping), which operate with greater efficiency deeper in the host potential. Essentially, if ram pressure is less effective at removing cold gas from an infalling dwarf, then the system will continue to form stars for several Gyr longer (yielding a longer  $\tau_{\text{quench}}$ ) relative to satellites of similar mass that are on more radial orbits and experience higher ram pressure.

## 4.2 Quenching in Ultra-Faint Dwarf Satellites

As highlighted in §1, the inferred SFHs of the ultra-faint dwarf galaxy population around the MW are universally consistent with a cessation of star formation at very early times (see also Martin et al. 2016, 2017). Recent work shows that these early quenching times are consistent with reionization being responsible for the suppression of star formation in the lowest mass galaxies (Brown et al. 2014; Rodriguez Wimberly et al. 2019). This is in good agreement with hydrodynamic simulations of isolated dwarfs, which find that reionization is effective in shutting down star formation on the smallest mass scales (Benítez-Llambay et al. 2015; Fitts et al. 2017; Jeon et al. 2017; Wheeler et al. 2018).

Our work adds further evidence to this reionization quenching scenario by determining the infall time for each of the UFDs with a measured SFH. Not only did star formation terminate at very early times, the inferred infall times for the UFDs occur after the SFH-based quenching time, strongly suggesting that quenching mechanisms associated with the MW environment are not the

dominant mode of star formation cessation. In agreement with simulations and related work, our analysis adds additional evidence for a stellar mass scale of  $M_{\star} \sim 10^5 M_{\odot}$ , below which star formation is shut down by reionization.

## 4.3 Comparison to Previous Studies

Utilizing the recently-measured 6D phase-space information for the MW satellites based on *Gaia* DR2 proper motions, we infer the infall time for 37 MW satellites through comparison to the phase-space distributions of subhalos in the pELVIS simulation suite. Previous work demonstrated the viability of this exercise using the Via Lactea simulations (Diemand et al. 2007, 2008) and showed the existence of a strong correlation between the binding energy and infall time for subhalos (Rocha et al. 2012). By applying a similar method to higher-resolution simulations that include a disk potential, we recover the same qualitative trends as those found by Rocha et al. (2012). However, the normalization, slope, and scatter of the correlation between binding energy and infall time varies from host to host. Additionally, previous work utilized only 4 components of the phase space for the majority of the MW dwarf galaxies and demonstrated that incorporating the full 6 components led to a stronger constraint on the infall time distribution (Rocha et al. 2012).

In our analysis, we are able to take advantage of the full phase-space measurements now available and a suite of simulations that better captures the host-to-host scatter in the properties of the subhalo population. Where applicable, the infall times in Rocha et al. (2012) and in this work agree within  $2\sigma$ . However, we generally infer earlier infall times. This difference is driven by the inclusion of the full 6D phase-space measurements based on *Gaia* proper motions. If we instead infer the infall time using only the Galactocentric position and radial velocity, then we find much better agreement (within  $1\sigma$ ) with Rocha et al. (2012). This agreement, however, does not imply accuracy, as the overall accuracy of this method decreases if we omit the tangential velocity component. When compared to the true infall times for subhalos in pELVIS, the inclusion of tangential motion to the estimate of  $t_{\text{infall}}$  reduces the catastrophic failure rate from  $\sim 30\%$  to  $\sim 20\%$ , where failure is defined to be  $|\Delta t_{\text{infall}}|/(1 + t_{\text{infall,true}}) > 0.2$ . Thus, when possible, the entire 6D phase space should be used to infer the most likely infall time for the MW dwarf galaxies.

Weisz et al. (2015) also characterize the quenching time for the MW satellite galaxies using *HST*-based star-formation histories. That work, however, was based on the less accurate infall times from Rocha et al. (2012), leading to the conclusion that many of the MW satellite galaxies with  $M_{\star} \gtrsim 10^5 M_{\odot}$  had their star formation shut down prior to becoming a satellite, in conflict with the established picture of environmental quenching. With the updated phase-space measurements from *Gaia* DR2, the infall times for these systems are now better constrained and favor a scenario in which environmental quenching dominates at  $M_{\star} \sim 10^{5-8} M_{\odot}$ .

## 5 SUMMARY

Our work highlights the power of combining detailed observations of galaxies in the nearby Universe with cosmological simulations. We characterize the infall time for the population of MW satellite galaxies with *Gaia* DR2 based proper motion measurements from Fritz et al. (2018). When combined with quenching times inferred from *HST*-based SFHs, we measure the quenching timescale for

individual satellites, facilitating a detailed, object-by-object study of satellite quenching. The principal results of our analysis are as follows:

- Using the Phat ELVIS suite of high-resolution, zoom-in simulations, we develop a mapping from binding energy to subhalo infall time that allows for relatively precise constraints on the infall time of MW satellites. As shown in Table 1, using this mapping, we estimate the infall time for all MW satellites with a *Gaia* DR2 proper motion measurement from Fritz et al. (2018) and currently reside within 300 kpc of the MW.
- The inferred quenching timescales for satellites of the Milky Way with  $M_{\star} = 10^{5-8} M_{\odot}$  is broadly consistent with the rapid cessation of star formation following infall, supporting the model for satellite quenching developed by Fillingham et al. (2015, 2016, 2018).
- The infall and quenching times measured for the UFD satellites of the MW are consistent with quenching via reionization and support a critical scale of  $M_{\star} \sim 10^5 M_{\odot}$  below which reionization is effective in suppressing star formation at early cosmic time.
- Within the sample of MW satellites studied (at  $M_{\star} < 10^8 M_{\odot}$ ), our measurements of infall and quenching times are fully consistent with quenching via reionization or environment, such that there is no need for satellites at these mass scales to be quenched due to internal processes – e.g. self-quenching via feedback.

## ACKNOWLEDGEMENTS

We thank Josh Simon and Alex Ji for useful conversations that helped shape some of this analysis. This work was supported in part by NSF grants AST-1815475, AST-1518257, AST-1517226, AST-1009973, and AST-1009999. Additional support was provided by NASA through grants AR-12836, AR-13242, AR-13888, AR-13896, GO-14191, and AR-14289 from the Space Telescope Science Institute, which is operated by the Association of Universities for Research in Astronomy, Inc., under NASA contract NAS 5-26555. MBK also acknowledges support from NSF CAREER grant AST-1752913 and NASA grant NNX17AG29G. Support for SGK was provided by an Alfred P. Sloan Research Fellowship, NSF Collaborative Research Grant #1715847 and CAREER grant #1455342, and NASA grants NNX15AT06G, JPL 1589742, 17-ATP17-0214 MSP acknowledges funding by NASA through Hubble Fellowship grant #HST-HF2-51379.001-A awarded by the Space Telescope Science Institute, which is operated by the Association of Universities for Research in Astronomy, Inc., for NASA, under contract NAS5-26555. CW was supported by the Lee A. DuBridge Postdoctoral Scholarship in Astrophysics.

This research has made use of NASA’s Astrophysics Data System Bibliographic Services. This research also utilized *Astropy*, a community-developed core Python package for Astronomy (*Astropy Collaboration et al. 2013*). Additionally, the Python packages *NumPy* (Walt et al. 2011), *iPython* (Pérez & Granger 2007), *SciPy* (Jones et al. 2001), *matplotlib* (Hunter 2007), and *scikit-learn* (Pedregosa et al. 2011) were utilized for our data analysis and presentation.

## REFERENCES

- Astropy Collaboration et al., 2013, *A&A*, 558, A33  
 Balogh M. L., et al., 2016, *MNRAS*, 456, 4364  
 Benítez-Llambay A., Navarro J. F., Abadi M. G., Gottlöber S., Yepes G., Hoffman Y., Steinmetz M., 2015, *MNRAS*, 450, 4207  
 Besla G., Kallivayalil N., Hernquist L., Robertson B., Cox T. J., van der Marel R. P., Alcock C., 2007, *ApJ*, 668, 949  
 Bland-Hawthorn J., Gerhard O., 2016, *ARA&A*, 54, 529  
 Blitz L., Robishaw T., 2000, *ApJ*, 541, 675  
 Boylan-Kolchin M., Ma C.-P., 2007, *MNRAS*, 374, 1227  
 Boylan-Kolchin M., Ma C.-P., Quataert E., 2008, *MNRAS*, 383, 93  
 Brown T. M., et al., 2014, *ApJ*, 796, 91  
 D’Onghia E., Springel V., Hernquist L., Keres D., 2010, *ApJ*, 709, 1138  
 Dark Energy Survey Collaboration et al., 2016, *MNRAS*, 460, 1270  
 Davies L. J. M., et al., 2016, *MNRAS*, 455, 4013  
 Diemand J., Kuhlen M., Madau P., 2007, *ApJ*, 667, 859  
 Diemand J., Kuhlen M., Madau P., Zemp M., Moore B., Potter D., Stadel J., 2008, *Nature*, 454, 735  
 Dierickx M. I. P., Loeb A., 2017, *ApJ*, 847, 42  
 Dolphin A., 1997, *New Astron.*, 2, 397  
 Efron B., 1982, The Jackknife, the Bootstrap and other resampling plans  
 El-Badry K., Wetzel A., Geha M., Hopkins P. F., Kereš D., Chan T. K., Faucher-Giguère C.-A., 2016, *ApJ*, 820, 131  
 Emerick A., Mac Low M.-M., Greevich J., Gatto A., 2016, *ApJ*, 826, 148  
 Fan X., et al., 2006, *AJ*, 132, 117  
 Fillingham S. P., Cooper M. C., Wheeler C., Garrison-Kimmel S., Boylan-Kolchin M., Bullock J. S., 2015, *MNRAS*, 454, 2039  
 Fillingham S. P., Cooper M. C., Pace A. B., Boylan-Kolchin M., Bullock J. S., Garrison-Kimmel S., Wheeler C., 2016, *MNRAS*, 463, 1916  
 Fillingham S. P., Cooper M. C., Boylan-Kolchin M., Bullock J. S., Garrison-Kimmel S., Wheeler C., 2018, *MNRAS*, 477, 4491  
 Fitts A., et al., 2017, *MNRAS*, 471, 3547  
 Fossati M., et al., 2017, *ApJ*, 835, 153  
 Fritz T. K., Battaglia G., Pawlowski M. S., Kallivayalil N., van der Marel R., Sohn S. T., Brook C., Besla G., 2018, *A&A*, 619, A103  
 Gaia Collaboration et al., 2016a, *A&A*, 595, A1  
 Gaia Collaboration et al., 2016b, *A&A*, 595, A2  
 Gaia Collaboration et al., 2018a, *A&A*, 616, A1  
 Gaia Collaboration et al., 2018b, *A&A*, 616, A12  
 Garrison-Kimmel S., Boylan-Kolchin M., Bullock J. S., Lee K., 2014, *MNRAS*, 438, 2578  
 Garrison-Kimmel S., et al., 2017, *MNRAS*, 471, 1709  
 Geha M., Blanton M. R., Yan R., Tinker J. L., 2012, *ApJ*, 757, 85  
 Gaus A. S., Bullock J. S., Kelley T., Boylan-Kolchin M., Garrison-Kimmel S., Qi Y., 2018, preprint, ([arXiv:1808.03654](https://arxiv.org/abs/1808.03654))  
 Gaus A. S., et al., 2019, preprint, ([arXiv:1901.05487](https://arxiv.org/abs/1901.05487))  
 Greevich J., Putman M. E., 2009, *ApJ*, 696, 385  
 Haines C. P., Gargiulo A., Merluzzi P., 2008, *MNRAS*, 385, 1201  
 Hunter J. D., 2007, *Computing In Science & Engineering*, 9, 90  
 Irwin M. J., 1994, in Meylan G., Prugniel P., eds, *European Southern Observatory Conference and Workshop Proceedings Vol. 49, European Southern Observatory Conference and Workshop Proceedings*. p. 27  
 Jeon M., Besla G., Bromm V., 2017, *ApJ*, 848, 85  
 Jones E., Oliphant T., Peterson P., et al., 2001, *SciPy: Open source scientific tools for Python*, <http://www.scipy.org/>  
 Kallivayalil N., van der Marel R. P., Besla G., Anderson J., Alcock C., 2013, *ApJ*, 764, 161  
 Kallivayalil N., et al., 2018, *ApJ*, 867, 19  
 Kelley T., Bullock J. S., Garrison-Kimmel S., Boylan-Kolchin M., Pawlowski M. S., Gaus A. S., 2018, preprint, ([arXiv:1811.12413](https://arxiv.org/abs/1811.12413))  
 Law D. R., Majewski S. R., 2010, *ApJ*, 714, 229  
 Lin D. N. C., Faber S. M., 1983, *ApJ*, 266, L21  
 Martin N. F., et al., 2016, *ApJ*, 833, 167  
 Martin N. F., et al., 2017, *ApJ*, 850, 16  
 Massari D., Helmi A., 2018, *A&A*, 620, A155  
 Mateo M. L., 1998, *ARA&A*, 36, 435  
 Navarro J. F., Frenk C. S., White S. D. M., 1997, *ApJ*, 490, 493

- Pace A. B., Li T. S., 2019, *ApJ*, **875**, 77
- Pedregosa F., et al., 2011, *Journal of Machine Learning Research*, **12**, 2825
- Pérez F., Granger B. E., 2007, *Computing in Science and Engineering*, **9**, 21
- Phillips J. I., Wheeler C., Cooper M. C., Boylan-Kolchin M., Bullock J. S., Tollerud E., 2015, *MNRAS*, **447**, 698
- Planck Collaboration et al., 2016, *A&A*, **594**, A13
- Purcell C. W., Bullock J. S., Tollerud E. J., Rocha M., Chakrabarti S., 2011, *Nature*, **477**, 301
- Robertson B. E., Ellis R. S., Furlanetto S. R., Dunlop J. S., 2015, *ApJ*, **802**, L19
- Rocha M., Peter A. H. G., Bullock J., 2012, *MNRAS*, **425**, 231
- Rodriguez Wimberly M. K., Cooper M. C., Fillingham S. P., Boylan-Kolchin M., Bullock J. S., Garrison-Kimmel S., 2019, *MNRAS*, **483**, 4031
- Sawala T., Pihajoki P., Johansson P. H., Frenk C. S., Navarro J. F., Oman K. A., White S. D. M., 2017, *MNRAS*, **467**, 4383
- Simon J. D., 2018, *ApJ*, **863**, 89
- Simpson C. M., Grand R. J. J., Gómez F. A., Marinacci F., Pakmor R., Springel V., Campbell D. J. R., Frenk C. S., 2018, *MNRAS*, **478**, 548
- Slater C. T., Bell E. F., 2014, *ApJ*, **792**, 141
- Spekkens K., Urbancic N., Mason B. S., Willman B., Aguirre J. E., 2014, *ApJ*, **795**, L5
- Tollerud E. J., Bullock J. S., Strigari L. E., Willman B., 2008, *ApJ*, **688**, 277
- Trussler J., Maiolino R., Maraston C., Peng Y., Thomas D., Goddard D., Lian J., 2018, preprint, ([arXiv:1811.09283](https://arxiv.org/abs/1811.09283))
- Walt S. v. d., Colbert S. C., Varoquaux G., 2011, *Computing in Science & Engineering*, **13**, 22
- Weinmann S. M., van den Bosch F. C., Yang X., Mo H. J., 2006, *MNRAS*, **366**, 2
- Weisz D. R., et al., 2011, *ApJ*, **739**, 5
- Weisz D. R., Dolphin A. E., Skillman E. D., Holtzman J., Gilbert K. M., Dalcanton J. J., Williams B. F., 2014, *ApJ*, **789**, 147
- Weisz D. R., Dolphin A. E., Skillman E. D., Holtzman J., Gilbert K. M., Dalcanton J. J., Williams B. F., 2015, *ApJ*, **804**, 136
- Weisz D. R., Dolphin A. E., Skillman E. D., Holtzman J., Gilbert K. M., Dalcanton J. J., Williams B. F., 2017, *VizieR Online Data Catalog*, **178**
- Wetzel A. R., Tinker J. L., Conroy C., van den Bosch F. C., 2013, *MNRAS*, **432**, 336
- Wetzel A. R., Deason A. J., Garrison-Kimmel S., 2015a, *ApJ*, **807**, 49
- Wetzel A. R., Tollerud E. J., Weisz D. R., 2015b, *ApJ*, **808**, L27
- Wheeler C., Phillips J. I., Cooper M. C., Boylan-Kolchin M., Bullock J. S., 2014, *MNRAS*, **442**, 1396
- Wheeler C., et al., 2018, preprint, ([arXiv:1812.02749](https://arxiv.org/abs/1812.02749))
- York D. G., et al., 2000, *AJ*, **120**, 1579

## APPENDIX A: INFALL TIME DISTRIBUTIONS

For completeness, we show the infall time distributions for every galaxy in our primary sample. See §2.2.4 for a description of how the observed properties of the MW satellites are matched to the subhalo population in the Phat ELVIS simulation suite, in order to infer the infall time for each MW satellite in our primary sample.

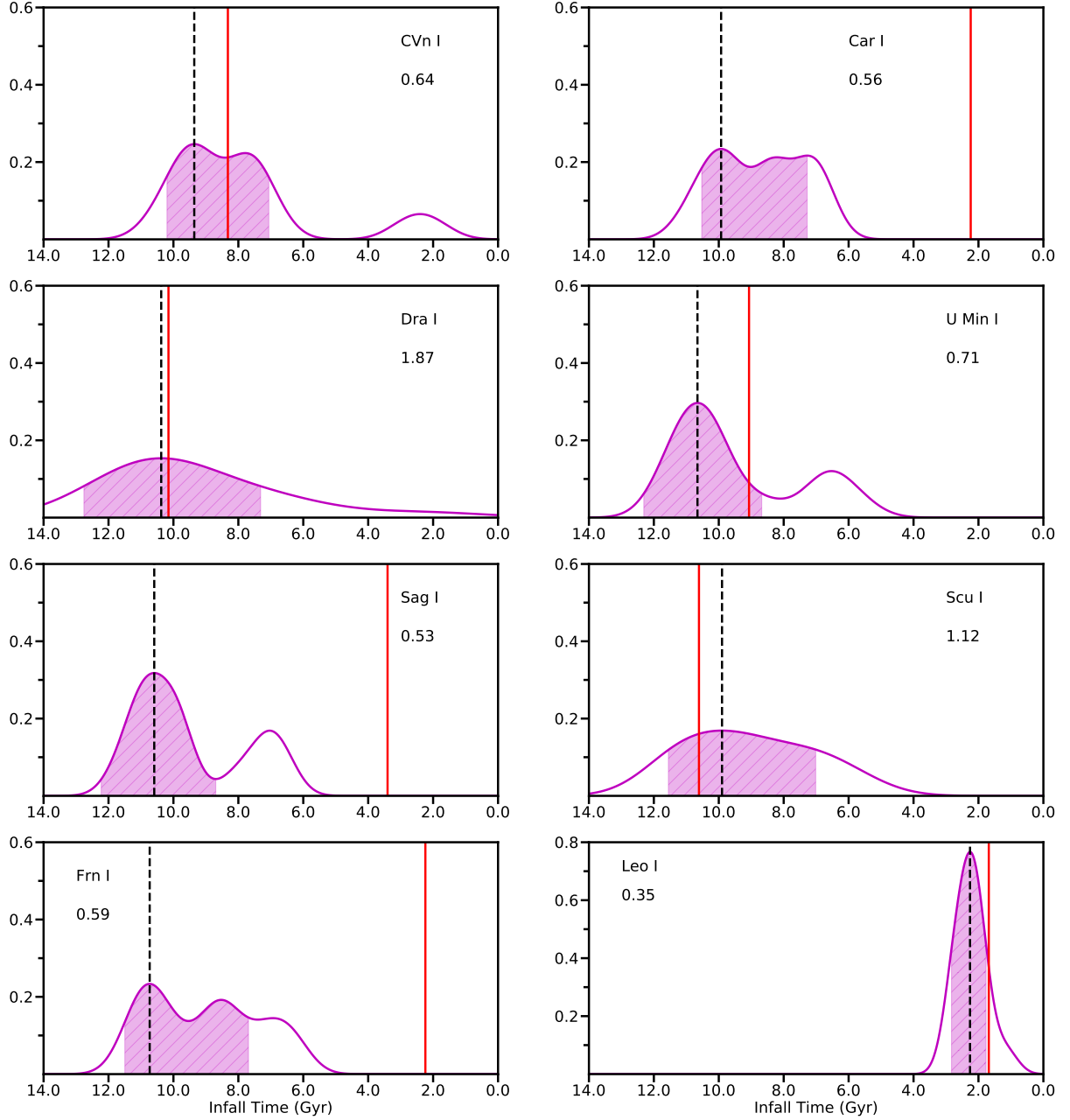


**Figure A1.** Same as the *right* panel of Figure 2 for the remaining “classical” MW satellite galaxies. The distribution of infall times for each respective MW satellite based on selecting the 15 closest subhalos in the  $\log(\mathcal{E}/V_{\max}^2)$ –host-centric distance space (see Fig. 1) and the same directionality in their radial velocity. The distribution of  $t_{\text{infall}}$  (magenta line) is smoothed with a gaussian kernel with a bandwidth chosen by a “leave-one-out” cross validation grid search, to allow for a cleaner inference of the peak of the distribution. The adopted bandwidth (in Gyr) is shown below each galaxy name in the respective panel. We adopt the peak in the distribution (black dashed line) as the characteristic infall time for each MW satellite. The accompanying magenta shaded region illustrates the adopted uncertainty on the characteristic  $t_{\text{infall}}$ , corresponding to the most probable region encompassing 68 % of the total distribution. For reference, the red line shows the quenching time as derived from the *HST*-based SFH.

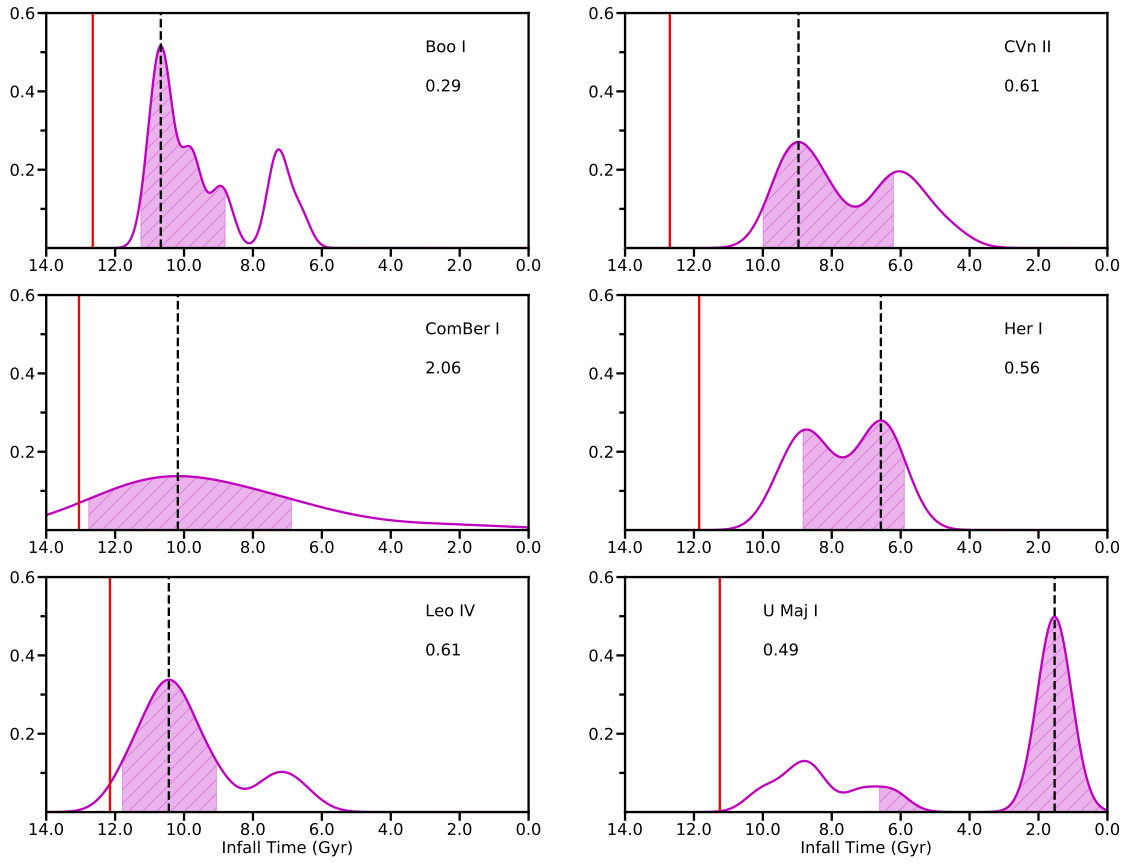


**Figure A2.** Same as Figure A1, except for the Ultra-Faint MW satellite galaxies (UFDs).